A&A 642, A145 (2020)
https://doi.org/10.1051/0004-6361/202039009

Astronomy & Astrophysics

A search for the OH 6035 MHz line in high-mass star-forming regions

M. Szymczak[1], P. Wolak[1], A. Bartkiewicz[1], M. Aramowicz[2], and M. Durjasz[1]

[1] Institute of Astronomy, Faculty of Physics, Astronomy and Informatics, Nicolaus Copernicus University, Grudziadzka 5, 87-100 Torun, Poland
e-mail: msz@astro.umk.pl
[2] Astronomical Institute, University of Wrocław, ul. Kopernika 11, 51-622 Wrocław, Poland

Received 23 July 2020 / Accepted 2 September 2020

ABSTRACT

Context. The excited states of OH masers detected in the environment of high-mass young stellar objects (HMYSOs) are important for improving our understanding of the physical conditions of these objects and also provide information about their magnetic fields.
Aims. We aim to search for excited-state OH 6035 MHz maser emission in HMYSOs which might have escaped detection in previous surveys or were never searched for.
Methods. A sample of HMYSOs derived from untargeted surveys of the 6668 MHz methanol maser line was observed at 6035 MHz OH transition with the Torun 32 m radio telescope. The 6035 MHz detections were observed in the OH 6031 MHz line. Two-thirds of the detections were observed at least three times over a two-year period.
Results. Out of 445 targets, 37 were detected at 6035 MHz, including seven new discoveries. The 6031 MHz line was detected towards ten 6035 MHz sources, one of which was not previously reported. All the newly detected sources are faint with the peak flux density lower than 4 Jy and show significant or high variability on timescales of 4 to 20 months. Zeeman pair candidates identified in three new sources imply a magnetic field intensity of 2–11 mG. Comparison of our spectra with those obtained ~10 yr ago indicates different degrees of variability but there is a general increase in the variability index on an ~25 yr timescale, usually accompanied by significant changes in the profile shape.

Key words. masers – stars: massive – stars: formation – ISM: molecules – radio lines: ISM

1. Introduction

Observations of spectral lines in the gas surrounding high-mass young stellar objects (HMYSOs) are one of the important tools to determine the physical and chemical conditions which enable the examination of mechanisms and star formation processes (Zinnecker & Yorke 2007). Maser lines are of special interest in this context as useful signposts of star formation activity (e.g. Menten 1991; Caswell 2003; Breen et al. 2015) which owing to their high levels of brightness and compactness can probe neutral gas cloudlets of a few tens of astronomical units (au) in size that reside in rotating structures such as toroids and discs (Beltrán & de Wit 2016) or around powerful jets (e.g. Anglada et al. 2018).

Ground-state OH maser transitions are one of the essential signatures of HMYSOs in their early stages of formation and have been detected in numerous sites (e.g. Caswell 1999; Forster & Caswell 1999; Argon et al. 2000; Edris et al. 2007; Beuther et al. 2019; Qiao et al. 2020). They are sometimes accompanied by the excited-state OH ($^2\Pi_{3/2}, J = 5/2$) transitions at 5 cm wavelength, where the main line 6035 MHz dominates in most cases (Yen et al. 1969; Knowles et al. 1976; Smits 1994; Caswell & Vaile 1995; Baudry et al. 1997; Caswell 2001, 2003; Avison et al. 2016). As this excited state of OH lies immediately above the ground state, it provides a critial test for maser pumping schemes (Baudry et al. 1997; Pavlakis & Kylafis 2000; Cragg et al. 2002). OH is a paramagnetic molecule, and therefore a significant Zeeman splitting is observed for the transitions, allowing reliable estimates of the magnetic field strength and its direction (Baudry et al. 1997; Caswell & Vaile 1995; Caswell 2003).

Most of past surveys of the excited-state OH maser transitions were commonly restricted to targets identified by ground-state OH masers (Caswell & Vaile 1995; Baudry et al. 1997) and obviously suffer from biases. Detection of the 6.7 GHz methanol line (Menten 1991), which is uniquely associated with star forming regions, opened a new path to identify more HMYSOs. Indeed, recent surveys of the 6.7 GHz line resulted in detection of several previously unknown HMYSOs, enlarging the number of candidates in early stages, where the massive star is still in an active phase of accretion and is deeply embedded in the parent molecular clouds (e.g. Green et al. 2010; Szymczak et al. 2012; Breen et al. 2015). Recently, the first complete untargeted survey of the accessible southern Galactic plane for the OH 6035 MHz line was carried out as part of the Methanol Multibeam Survey (MMB, Avison et al. 2016, 2020). In this paper we report the results of the OH 6035 MHz survey of HMYSO candidates with which we aim to expand the sample of excited-state OH sources, particularly for the northern hemisphere, and to search for sources that may have escaped detection in previous observations due to variability. Observations of excited-state OH masers may allow us to find targets for multi-line maser studies with high angular resolution.

2. Observations

Observations of the $^2\Pi_{3/2}, J = 5/2, F = 3-3$ OH transition at 6035.092 MHz were carried out from June to September 2018 with the Torun 32 m radio telescope. Detections were reobserved in two sessions: November-December 2018 and

Table 1. 6035 GHz OH line parameters for the new detections.

Name (l b)	RA (J2000)	Dec (J2000)	ΔV	LHC			RHC		
				$V_{\rm p}$	$S_{\rm p}$	$S_{\rm i}$	$V_{\rm p}$	$S_{\rm p}$	$S_{\rm i}$
(° °)	(h m s)	(° ′ ″)	(km s^{-1})	(km s^{-1})	(Jy)	(Jy km s^{-1})	(km s^{-1})	(Jy)	(Jy km s^{-1})
G12.209−00.102	18 12 39.92	−18 24 17.9	16.0;18.2	16.97	1.78	1.41	17.35	2.47	1.14
G25.710+00.044	18 38 03.15	−06 24 14.9	93.6;96.0	95.52	1.12	0.93	95.45	0.85	0.90
G28.146−00.005	18 42 42.59	−04 15 36.5	101.0;101.6	101.38	1.27	0.35	101.42	2.89	0.73
G85.410+00.003	20 54 13.68	+44 54 07.6	−33.3;−32.7	−32.92	0.74	0.30	−32.97	2.00	0.61
G90.921+01.486	21 09 12.98	+50 01 03.6	−70.5;−68.4	−69.24	1.00	0.66	−69.20	1.89	0.81
G108.766−00.986	22 58 51.18	+58 45 14.4	−46.3;−44.7	−45.37	0.95	0.49	−45.95	2.21	1.21
G183.348−00.575	05 51 10.94	+25 46 17.2	−6.1;−5.0	−5.30	3.68	1.13	−5.29	0.78	0.20
G183.348−00.575 [a]	05 51 10.94	+25 46 17.2	−5.4;−4.9	−5.15	1.27	0.27		<0.61 [b]	<0.05

Notes. The velocity range of I Stokes emission (ΔV), the peak velocity ($V_{\rm p}$), peak flux density ($S_{\rm p}$), and integrated flux density ($S_{\rm i}$) for the LHC and RHC polarisation are given. [a]6031 MHz transition, [b]3σ level.

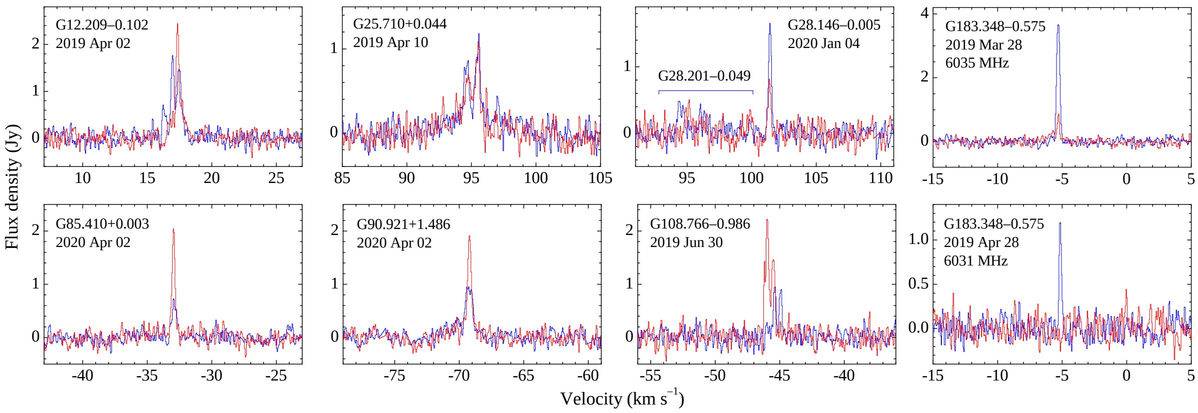

Fig. 1. 6035 MHz OH maser spectra of newly detected sources from the Torun observations. The new detection of the 6031 MHz transition for one target is also shown. Blue and red lines denote LHC and RHC polarisation, respectively. Observation dates are given.

March-April 2019, and since then several sources have been monitored. Furthermore, all of them were also searched for the $^2\Pi_{3/2}, J=5/2, F=2-2$ line at 6030.747 MHz. The telescope has a half-power beam width of 6′.4 at these frequencies and the pointing accuracy was about 10″. The observations were pointed on the positions of 6668 MHz methanol maser sources whose coordinates are known with sub-arcsecond accuracy in almost all cases. The sample includes all the methanol masers from the Torun catalogue (Szymczak et al. 2012) updated with objects above declination −22° from the Multibeam Methanol Survey (Green et al. 2010; Breen et al. 2015). The targets were observed in left- and right-hand circular (LHC and RHC) polarisation simultaneously using a dual-channel receiver system with the system temperature ranging from 25 to 30 K. The IEEE convention for the handedness of polarisation was adopted and Stokes V parameter was defined following the IAU convention as $V = S\,(\mathrm{RHC}) - S\,(\mathrm{LHC})$, where S (RHC) and S (LHC) are the line flux densities for right and left circular polarisation, respectively. Spectra were obtained with an autocorrelation spectrometer in the frequency-switching mode using two banks of 4096 channels each, covering a velocity range of 95 km s^{-1} with a velocity resolution of 0.1 km s^{-1} after Hanning smoothing. The spectra were centred at the middle velocity of the methanol maser profiles measured relative the local standard of rest. Typical integration lasted 20 min resulting in an rms noise level of 0.20–0.25 Jy for a single polarisation flux density. Parameters of the receiving system were regularly measured through observations of continuum and spectral line calibrators as described in Szymczak et al. (2012). The gain of each polarisation channel was measured with a noise diode at the beginning of each ninety-second integration cycle to ~10% in absolute value and to within ~4% in relative value. The degree of circular polarisation is defined as $m_{\rm C} = V/I$, where V and I are Stokes parameters of circularly polarised emission and total emission, respectively.

3. Results

Among 445 targets observed, the 6035 MHz emission was detected in 37 objects of which 7 are new detections. The 6031 MHz emission was detected towards ten 6035 MHz objects. The parameters of spectra of new and known sources ordered by galactic longitude are listed in Tables 1 and A.1, respectively. The spectra of new detections are shown in Fig. 1 and those of known sources are in Fig. A.1. A list of non-detections is provided in Table A.2.

The following notes provide information on a possible association of the 6035 MHz emission with the 6668 MHz masers on the basis of velocities of their maser peaks and systemic velocity of the parent molecular clouds. Estimates of the magnetic field strength of some of the masers and comments on the degree of circular polarisation are also given.

G12.209−00.102. The 6035 MHz maser emission detected in a velocity range of 16–18.5 km s^{-1}, with $|m_{\rm C}| \approx 30$–40% for the strongest features, is ~5 km s^{-1} blueshifted from OH 1665 MHz maser features (Argon et al. 2000) but coincides well with the 6668 MHz methanol emission range (Green et al. 2010). The 1665 MHz emission lies within less than 2″ from the methanol maser (Argon et al. 2000; Caswell 2009) and at this position there are five methanol masers (Caswell 2009; Green et al. 2010) in the telescope beam. The 6035 MHz spectrum shows strong variability (Sect. 4.4) preserving possible Zeeman splitting which corresponds to a magnetic field of +2.6 to +8.8 mG (Table A.3).

G25.709+00.044. The 6035 MHz maser shows weakly polarised emission with double peaks around 95 km s^{-1}. Avison et al. (2016, 2020) reported an almost identical 6035 MHz spectrum towards G25.509−0.060 which these latter authors referred to as an isolated excited-state OH source because it has no 6668 MHz methanol maser within >6′.5, or 22 μm WISE counterpart within 1′.2, or 1.1 mm ATLASGAL emission within 2′. At this position we did not find 6035 MHz emission with upper limit of 0.5 Jy in 2020 April while the intensity towards G25.710+0.044 was 0.9 Jy(>4σ) at the same epoch confirming this as a new detection.

G28.146−00.005. The 6035 MHz spectrum contains a narrow feature at 101.4 km s^{-1} which is significantly polarised (m_C = 40%) and exactly coincides in velocity with the strongest feature of the 6668 MHz maser (Breen et al. 2015). In our spectrum, a side-lobe emission from G28.201−0.049 is seen at a velocity lower than 96.5 km s^{-1} (Caswell & Vaile 1995; Baudry et al. 1997).

G85.410+0.003. The 6035 MHz spectrum is markedly polarised (m_C = 54%) and the peak velocity lies at the low-velocity edge of the CH_3OH and H_2O maser spectra (Szymczak et al. 2012; Urquhart et al. 2011) very close to the systemic velocity of −35.8 km s^{-1} derived from NH_3 lines (Urquhart et al. 2011). This new source is associated with an embedded stellar cluster of very young stars (Persi et al. 2011) where the 6668 MHz maser coincides within 0′.3 with a compact HII region detected at centimetre wavelengths (Urquhart et al. 2009; Hu et al. 2016).

G90.921+1.486. This source has 6035 MHz polarised emission (m_C = 38%) at the same velocity as the most red-shifted feature, −69.2 km s^{-1}, of the 6668 MHz methanol maser (Szymczak et al. 2012). A tentative absorption feature centred at −73.5 km s^{-1} is seen. A weak feature of the OH 1667 MHz (Szymczak & Kus 2000) was blueshifted by 3.3 km s^{-1} from the 6035 MHz feature. The methanol maser is associated with a compact HII region (Hu et al. 2016).

G108.766−00.986. Double components of 6035 MHz maser emission are seen at the exact velocity of the strongest 6668 MHz maser feature at −46.6 km s^{-1} (Szymczak et al. 2012). These are blueshifted by 6 km s^{-1} from the systemic velocity and H_2O maser velocity range (Urquhart et al. 2011). There is a consistent Zeeman pair seen for the whole emission implying a magnetic field of −10 mG.

G183.348−00.575. A highly polarised feature (m_C = −65%) is detected at a velocity of −5.3 km s^{-1}. The strongest 6668 MHz methanol feature is seen at nearly the same velocity (Szymczak et al. 2012). The OH 6035 MHz emission is red-shifted by 4.3 km s^{-1} from the systemic velocity (Wu et al. 2010). Newly detected 6031 MHz emission closely matches the main 6035 MHz feature; it is completely polarised and has the narrowest profile with a width to half intensity of only 0.21 km s^{-1}.

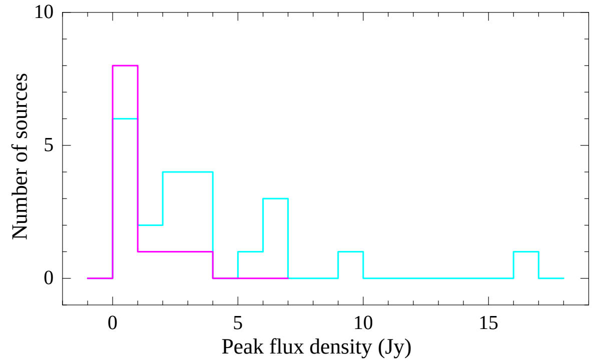

Fig. 2. OH 6035 MHz peak flux of sources in the Galactic longitude range 8° to 60° from the Avison et al. (2016) MMB survey. The OH sources coincide with 6.7 GHz methanol masers within 10″. The histograms show OH detection (cyan) and non-detection (magenta) in the present survey.

4. Discussion

4.1. Detection rate and methanol/hydroxyl luminosity ratio

In the Galactic longitude of 8−60°, our survey overlaps with the MMB untargeted observations and there are 375 methanol masers at 6.7 GHz (Green et al. 2010; Breen et al. 2015) of which 33 (8.8%) have an OH 6035 MHz maser counterpart within <10″ (Avison et al. 2016). There are also ten OH sources without a methanol counterpart within 10″. In the present observation of this area the number of OH sources associated (within 10″) with the methanol maser decreased to 22 (5.9%). The three new OH sources are not taken into account because with the beam of 6′.4 we were not able to discern whether or not they meet the above criterion of coincidence with the methanol masers. As a consequence of slightly lower sensitivity (by ∼25%), our detection rate is lower than that inferred from the MMB survey. Similar to previous studies (Avison et al. 2016, 2020), we find that the OH 6035 MHz maser emission is rather sparsely associated with the sources of the 6.7 GHz maser line. This implies that coexistence of 6.7 GHz methanol and 6035 MHz hydroxyl masers traces rather uncommon physical conditions with a narrow range of gas density of about 10^8 cm^{-3} and low kinetic temperature of <50 K (Cragg et al. 2002). High-angular-resolution studies are required in order to decipher whether or not these transitions come from the same gas volume.

Figure 2 shows the distribution of peak flux density of 33 OH masers at epochs (2008-2009) of MMB observations (Avison et al. 2016) in the overlapped area. The six OH sources found by these latter authors with peak flux density above our sensitivity limit of 0.7 Jy are not detected, while their 5 OH sources below this threshold are seen in the present survey. This implies considerable variability of 6035 MHz transition on a timescale of ∼10 yr; this point is further discussed in Sect. 4.4.

In the 8−60° region we found four OH masers which coincide within less than 0′.5 with the 6.7 GHz sources and show distinct emission at the same velocities. Using the methanol unpublished spectra taken with the Torun 32 m telescope (Szymczak et al. 2018) at almost the same epochs (±3 days), we calculated the ratio of 6.7 GHz to 6.035 MHz isotropic luminosity for the OH velocity range. For two features of G15.034−00.677 centred at 21.4 and 23.5 km s^{-1} this ratio is 1.9 and 2.6, respectively, while for the strongest OH features of G20.237+00.065 and G35.025+00.350 it is 2.5 and 3.1, respectively, and in

G11.904−00.141 the ratio is 30.5. It is surprising that in the three objects, the luminosity of the 6.7 GHz line is only a factor of two to three higher than that of the 6.035 MHz line. This may suggest very specific conditions, for instance where the methanol maser is quenched due to collisions in high-density gas while the OH 6.035 MHz maser is still excited (Cragg et al. 2002). We stress that our estimates need to be verified with high-angular-resolution observations to confirm whether or not both transitions are really co-spacial.

4.2. Line width

For all spectral features with a signal-to-noise ratio (S/N) greater than five we fitted Gaussian components to estimate the line parameters. We identify 61 LHC and 66 RHC spectral features of previously known sources and 11 features at both polarisations of new detections at the 6035 MHz transition. We also find 10 LHC and 11 RHC components at the 6031 MHz transition for known sources and one LHC component for the new detection. The full width at half maximum (FWHM) at 6035 MHz ranges from 0.16 to 0.95 km s^{-1} and the mean and median values are 0.41 ± 0.05 and 0.36 km s^{-1}, respectively. These values are larger by a factor of 1.8 than those inferred from high-angular-resolution data (Desmurs et al. 1998; Fish & Sjouwerman 2007). This discrepancy is likely due to spatial filtering out of the emission in VLBI observations where the brightest, most compact maser cloudlets are seen and the line width is lower as compared to single dish spectra. Another possibility is that Gaussian fitting failed for blended spectra obtained with our moderate sensitivity. The mean and median values of FWHM at 6031 MHz are 0.33 ± 0.06 and 0.36 km s^{-1} and are consistent with those for the 6035 MHz transition. This supports the conclusions of previous studies (e.g. Baudry et al. 1997; Fish & Sjouwerman 2007). For the new detection of 6031 MHz emission, the FWHM of the isolated component is 0.21 km s^{-1}. We did not find any correlation between line width and flux density.

4.3. Zeeman pair candidates

We used the convention that a field directed away from the observer has a positive sign and is indicated by the RHC component at more positive velocity that the LHC component. The following coefficients were used for the magnetic field strength estimation derived from the velocity separation of each pair: ΔV (km s^{-1}) /H(mG) = 0.056 and 0.079 at 6035 MHz and 6031 MHz, respectively (Baudry et al. 1997).

Zeeman pairs were categorised based on a comparison of the Gaussian fits of the spectral components (Sect. 4.2). The fitted peak velocities and FWHM values but no peak amplitudes were used for comparison. For complex spectra, only the prominent spectral components were considered to match pairs of components with nearby velocities and opposite senses of polarisation. We neglected pairs with one component lying on the edge of the other component.

We identified 34 LHC/RHC pairs at the 6035 MHz and 9 pairs at the 6031 MHz transition; see Table A.3, where we also list the fitted peak velocities and flux densities, demagnetized velocities, field strength, reliability of Zeeman pair identification, and field strength from the literature. The inferred magnetic field ranges from 0.1 to 12.0 mG as indicated by the splitting of the 6035 MHz line and from 0.2 to 9.0 mG of the 6031 MHz line. The mean and median values are 4.6 and 4.4 mG (6035 MHz), and 4.6 and 3.9 mG (6031 MHz).

The possible Zeeman pairs listed in Table A.3 should be treated with care, especially those labelled “B”. All the pairs need to be verified with high-angular-resolution observations to definitively demonstrate that the candidate Zeeman pairs spatially coincide and are thus genuinely associated. Nevertheless, our estimates of the magnetic field seem to be consistent with those reported in the literature (Table A.3); in most cases, we obtained similar field strength and in all cases the same field direction.

Caswell (1997) pointed out that there was no field greater than about 10 mG. Therefore, it will be important to verify, using interferometric data, the magnetic field strengths in G12.681−00.182, G69.540−00.976, and G108.7666−00.986, where our estimated values exceeded 10 mG. Moreover, in G15.035−00.677, G45.467+00.053, and G80.861+00.383 the field reversal is seen and follow-up studies would be desirable to uncover the magnetic field morphology.

Three objects (G11.034+00.062, G11.904−00.141 and G15.035−00.677) were observed in full polarisation by Green et al. (2015). For the first two sources, our estimates of the magnetic field strength are only roughly (35%) consistent with the values of these latter authors (Table A.3). This could be due to the fact that our spectra are much noisier than theirs. In the case of the bright source G15.035−00.677 whose 6031 MHz profile was identified as a Zeeman triplet candidate (Green et al. 2015), we obtained field strengths similar to those reported in the literature (Table A.3).

4.4. Variability

Most of our newly detected sources were observed three or more times over a period of less than two years. To quantify their variability we used the variability index given by

$$vi = \frac{(S_{\max} - \sigma_{\max}) - (S_{\min} + \sigma_{\min})}{(S_{\max} - \sigma_{\max}) + (S_{\min} + \sigma_{\min})} \quad (1)$$

which is a measure of the amplitude of the variability of the spectral feature. Here, $S_{\max}$ and $S_{\min}$ are the highest and lowest measured flux densities, respectively, and $\sigma_{\max}$ and $\sigma_{\min}$ are the uncertainties in these measurements. The variability index for the strongest features on a timescale of nearly two years, vi_2, is listed in Table 2. We restrict our analysis to sources with a peak flux density greater than 1 Jy to eliminate spurious effects. For previously known objects, we estimated the variability indices relative to the 2008–2009 measurements of Avison et al. (2016) (vi_{10}) and the 1993–1994 observations by Caswell & Vaile (1995) (vi_{25}). These variability indices are added to Table 2 and for sources with complex spectra the velocity and polarisation of the considered feature are given in the notes.

Of 25 sources with reliably estimated vi_2, 8 show little or no variation within the noise, 12 show moderate or significant variability ($0.1 < vi_2 < 0.3$), and 5 sources show large variability, that is, a factor of ≥2 ($vi_2 > 0.3$). We note that all the newly detected sources show significant or high variability. We suggest that the considerable variability of G12.209−00.102, G25.710+0.044, and G28.146−0.005 is the cause of the non-detection in the more sensitive MMB survey (Avison et al. 2016).

The variability index of the main feature does not give the complete picture of variability for sources with complex spectra. Figure 3 shows the spectra of G12.209−00.102 at three epochs spanning almost 9 months. In July and December 2018, the shape of the spectrum in the velocity range of 15.5–20.2 km s^{-1} was preserved but it was completely rebuilt in April 2019 when the intensity decreased by a factor of seven and polarisation properties changed remarkably. Clearly detected emission at velocities higher than 24.7 km s^{-1} with a peak flux of 2.7 Jy appeared only

Table 2. Variability indices of 6035 MHz emission for the main feature on timescales of 2 (vi_2), 10 (vi_{10}), and 25 (vi_{25}) years.

Source	vi_2	vi_{10}	vi_{25}
G10.320−00.259	0.04	0.02	
G10.958+00.022	0.02	0.12	
G11.034+00.062	0.04	0.03	0.79
G11.904−00.141	0.30	0.78	0.78
G12.209−00.102	0.72		
G12.681−00.182	0.42	0.73	
G15.035−00.677 [(1),(2)]	0.06	0.40	0.48
G20.237+00.065	0.30	0.24	0.35
G24.148−00.009	0.34	0.54	
G25.650+01.049	0.03	0.09	
G25.710+00.044	0.21		
G28.146−00.005	0.25		
G28.201−00.049		0.31	0.34
G30.771−00.804		0.08	
G34.257+00.153 [(3),(2)]		0.46	0.70
G34.267−00.210	0.02		
G35.025+00.350	0.18	0.26	0.44
G43.149+00.013	0.12	0.16	0.44
G45.467+00.053 [(4)]	0.02	0.10	0.20
G48.990−00.299	0.16	0.20	
G49.490−00.388 [(5),(2)]	0.02	0.24	0.67
G80.861+00.383	0.39		
G81.871+00.781 [(6)]	0.18		
G85.410+00.003	0.17		
G108.766−00.986	0.22		
G111.542+00.777	0.28		
G133.947+01.064 [(7)]	0.11		
G183.348−00.575	0.53		

Notes. For sources with complex spectra, the velocity and polarisation of the feature used are noted. New detections are in bold. [(1)]21.5 km s^{-1} LHC; [(2)]large changes in the spectrum shape; [(3)]58.4 km s^{-1} RHC; [(4)]66.38 km s^{-1} LHC; [(5)]55.0 km s^{-1} RHC; [(6)]7.87 km s^{-1} RHC; [(7)]−43.3 km s^{-1} LHC.

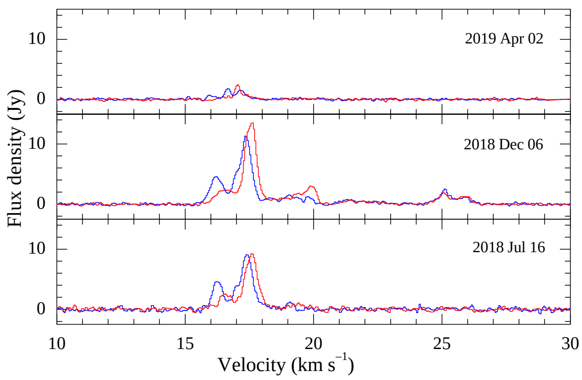

Fig. 3. OH 6035 MHz spectra of G12.209−00.102 at three epochs. Blue and red lines denote LHC and RHC polarisation, respectively.

in December 2018. This case proves that remarkable variations of OH 6035 MHz emission occur on timescales of less than 4 months. No significant variations in a 6 month interval were reported by Caswell & Vaile (1995).

A general trend can be seen in terms of an increase in variability index with increasing timescales (Table 2). Figure 4 shows the light curve of the main feature in G15.035−00.677.

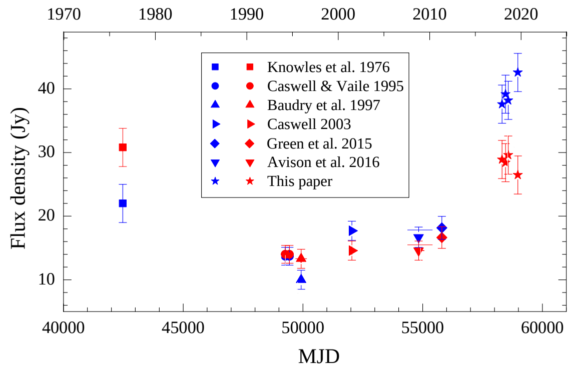

Fig. 4. Long term variability of the main feature (21.5 km s^{-1}) of G015.035−00.677 at 6035 MHz. Blue and red symbols denote LHC and RHC polarisation, respectively.

The first published spectrum with the flux density scale was obtained in 1975 (Knowles et al. 1976) and contains two spectral features; the most prominent of the two corresponds to our 21.45 km s^{-1} feature and the emission in RHC polarisation was stronger than that in LHC polarisation. The RHC flux density of this latter feature decreased by a factor of 2.2 after 18.6 yr (Caswell & Vaile 1995), and then remained stable within 15% over a period of 18 yr and increased by a factor of two after 10 yr. The LHC flux density followed the same course. During a low plateau state the difference between polarisation diminished and then the LHC signal became dominant. The flux ratio of the 21.45 and 22.65 km s^{-1} features varied from 1.8 (Knowles et al. 1976) to 0.96 (Caswell 2003) and then to 2.1 during our observations. The case of G15.035−00.677 depicts significant variations in the intensity, spectrum shape, and polarisation over a period of 45 yr. We note significant changes on a similar timescale for the 6035 and 6031 MHz masers of G133.947+01.064 (W3OH) when comparing our spectra with those reported in the literature (e.g. Moran et al. 1978; Desmurs & Baudry 1998; Fish & Sjouwerman 2007).

4.5. Unusual flux ratio in G49.490−00.388

Towards the G49.490−00.388 site, the OH emission near the velocity of 52.4 km s^{-1} shows striking characteristics; the 6031/6035 MHz flux density ratio exceeds unity for almost the total width of the profile, reaching a peak value of 3.4 and 3.1 for LHC and RHC polarisation, respectively (Fig. 5). This phenomenon in the source was discussed by Caswell (2003) who also noted similar properties in G345.010+01.792 and G353.410−00.360 observed by Smits (1994), but in the first of them this feature was short lived (Caswell 2003). Baudry et al. (1997) noted the well-known source G109.871+2.114 (Cep A) as the exceptional case with the 6031/6035 flux ratio of order unity. This source probably shows significant variability and was not detected in the present survey.

In G49.490−00.388, the line profiles of both transitions match in velocity and polarisation. A magnetic field strength derived from the velocity separation of peaks in each sense of circular polarisation is +4.8 ± 0.3 and +5.2 ± 0.4 mG for 6031 and 6035 MHz, respectively, and is consistent with that observed ∼18 yr ago but at a velocity near 53.2 km s^{-1} (Caswell 2003). Avison et al. (2016) reported the MMB observations taken in 2008–2009 where 6031 MHz RHC polarised emission at 52.7 km s^{-1} is stronger by a factor of 1.3 than the counterpart emission at 6035 MHz. The data from 1994 suggest a similar flux ratio (Baudry et al. 1997; Desmurs & Baudry 1998). In

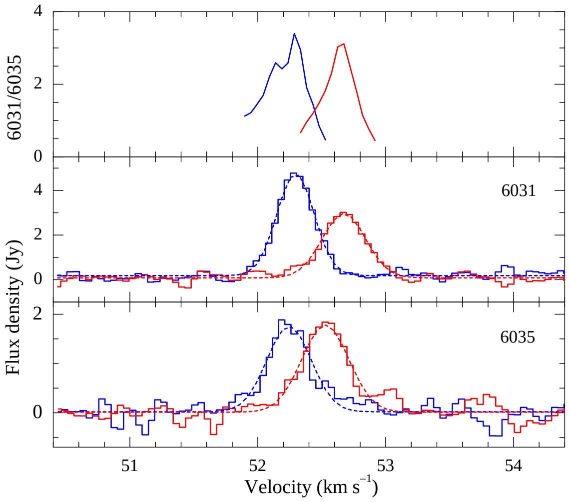

Fig. 5. Part of OH spectra in G49.490−00.388 showing a rare case where the maser intensity at 6031 MHz surpasses that at 6035 MHz. *Upper panel*: line ratio for each polarisation. Blue and red lines are LHC and RHC polarisation, respectively. The dashed lines correspond to the Gaussian fits.

turn, the spectra from 1973 imply a ratio of 0.6 and 0.4 for the LHC and RHC polarisation, respectively, when the profiles were seen near 53.2 km s^{-1} (Rickard et al. 1975). The magnetic field strength estimates at that epoch of +4.1 to +5.7 mG are fully consistent with ours. We conclude that the flux ratio of the feature varies considerably, exceeding unity for a period of at least 25 yr. This emission appeared at slightly different velocities and the spectra taken at four epochs: 1994 (Baudry et al. 1997; Desmurs & Baudry 1998), 2001 (Caswell 2003), 2008-2009 (Avison et al. 2016), and 2019 (this paper) suggest a velocity drift of 0.03 km s^{-1} yr^{-1}.

High-angular-resolution observations of a few sources revealed a good match of positions between the 6031 and 6035 MHz maser components (Desmurs & Baudry 1998; Desmurs et al. 1998; Etoka et al. 2005) suggesting co-propagation of both lines. According to model calculations, these transitions probe the gas for low gas temperature (<70 K), high density ($3\times10^{7-8}$ cm^{-3}), and OH column densities greater than 2×10^{17} cm^{-2} (Cragg et al. 2002). In the models of these latter authors, the 6031 MHz line closely accompanies the 6035 MHz line but is usually weaker. This prediction is consistent with observations for which the typical value of the peak flux ratio of 6031/6035 ranges from 0.14 to 0.5 (Baudry et al. 1997; Caswell 2003; Avison et al. 2016). Thus, the excess of 6031 MHz emission in G49.490−00.388 could be produced under some special conditions that could be extremely rare or transient (Caswell 2003) and that have not been explored in models. As the ratio increased over more than four decades and the profile slightly drifts in velocity, the maser may emerge from a region accelerated by stellar wind or outflow where physical conditions are readily deviating from typical parameters tested in the maser models (Cragg et al. 2002).

5. Conclusions

The detection rate of excited-state OH transition of 6% implies a rare association of OH 6035 MHz and CH_3OH 6668 MHz masers. Nevertheless, we identified three objects with possible co-propagation of both transitions. For these sources, the ratio of CH_3OH/OH isotropic luminosities is only between two and three and may indicate the gas cloudlets with a narrow range of gas density of about 10^8 cm^{-3} and low kinetic temperature of <50 K. This possibility needs to be examined with high-angular-resolution observations.

All the newly detected OH maser sources show variability greater than a factor of 1.4–6.1 on timescales of 4–20 months while their non-detection in previous more sensitive surveys suggests extraordinary variations on timescales of several years. For previously known sources, we saw a general trend of an increase in variability index for longer (10–25 yr) timescales.

A rare case of a source with the maser intensity at 6031 MHz surpassing that at 6035 MHz was confirmed. Inspection of the available data revealed one feature with considerable variations of the 6031/6035 flux ratio, exceeding unity for a period of 25 yr. This phenomenon cannot be explained by the standard models but observational characteristics such as a drift in velocity suggest that it occurs in a region accelerated by stellar wind or outflow. Further monitoring and interferometric studies are required to understand this unusual case.

Acknowledgements. The 32 m radio telescope is operated by the Institute of Astronomy, Nicolaus Copernicus University and supported by the Polish Ministry of Science and Higher Education SpUB grant. We thank the staff and students for assistance with the observations. This research has made use of the SIMBAD data base, operated at CDS (Strasbourg, France) and NASA's Astrophysics Data System Bibliographic Services. We acknowledge support from the Polish National Science Centre grant 2016/21/B/ST9/01455.

References

Anglada, G., Rodríguez, L. F., & Carrasco-González, C. 2018, A&ARv, 26, 3
Argon, A. L., Reid, M. J., & Menten, K. M. 2000, ApJS, 129, 159
Avison, A., Quinn, L. J., Fuller, G. A., et al. 2016, MNRAS, 461, 136
Avison, A., Quinn, L. J., Fuller, G. A., et al. 2020, MNRAS, 495, 3839
Baudry, A., Desmurs, J. F., Wilson, T. L., & Cohen, R. J. 1997, A&A, 325, 255
Beltrán, M. T., & de Wit, W. J. 2016, A&ARv, 24, 6
Beuther, H., Walsh, A., Wang, Y., et al. 2019, A&A, 628, A90
Breen, S. L., Fuller, G. A., Caswell, J. L., et al. 2015, MNRAS, 450, 4109
Caswell, J. L. 1997, MNRAS, 289, 203
Caswell, J. L. 1999, MNRAS, 308, 683
Caswell, J. L. 2001, MNRAS, 326, 805
Caswell, J. L. 2003, MNRAS, 341, 551
Caswell, J. L. 2009, PASA, 26, 454
Caswell, J. L., & Vaile, R. A. 1995, MNRAS, 273, 328
Cragg, D. M., Sobolev, A. M., & Godfrey, P. D. 2002, MNRAS, 331, 521
Desmurs, J. F., & Baudry, A. 1998, A&A, 340, 521
Desmurs, J. F., Baudry, A., Wilson, T. L., Cohen, R. J., & Tofani, G. 1998, A&A, 334, 1085
Edris, K. A., Fuller, G. A., & Cohen, R. J. 2007, A&A, 465, 865
Etoka, S., Cohen, R. J., & Gray, M. D. 2005, MNRAS, 360, 1162
Fish, V. L., & Sjouwerman, L. O. 2007, ApJ, 668, 331
Forster, J. R., & Caswell, J. L. 1999, A&AS, 137, 43
Green, J. A., Caswell, J. L., Fuller, G. A., et al. 2010, MNRAS, 409, 913
Green, J. A., Caswell, J. L., & McClure-Griffiths, N. M. 2015, MNRAS, 451, 74
Hu, B., Menten, K. M., Wu, Y., et al. 2016, ApJ, 833, 18
Knowles, S. H., Caswell, J. L., & Goss, W. M. 1976, MNRAS, 175, 537
Menten, K. M. 1991, ApJ, 380, L75
Moran, J. M., Reid, M. J., Lada, C. J., et al. 1978, ApJ, 224, L67
Pavlakis, K. G., & Kylafis, N. D. 2000, ApJ, 534, 770
Persi, P., Tapia, M., & Gómez, M. 2011, A&A, 525, A1
Qiao, H.-H., Breen, S. L., Gómez, J. F., et al. 2020, ApJS, 247, 5
Rickard, L. J., Zuckerman, B., & Palmer, P. 1975, ApJ, 200, 6
Smits, D. P. 1994, MNRAS, 269, L11
Szymczak, M., & Kus, A. J. 2000, A&AS, 147, 181
Szymczak, M., Wolak, P., Bartkiewicz, A., & Borkowski, K. M. 2012, Astron. Nachr., 333, 634
Szymczak, M., Olech, M., Sarniak, R., Wolak, P., & Bartkiewicz, A. 2018, MNRAS, 474, 219
Urquhart, J. S., Hoare, M. G., Purcell, C. R., et al. 2009, A&A, 501, 539
Urquhart, J. S., Morgan, L. K., Figura, C. C., et al. 2011, MNRAS, 418, 1689
Wu, Y. W., Xu, Y., Pandian, J. D., et al. 2010, ApJ, 720, 392
Yen, J. L., Zuckerman, B., Palmer, P., & Penfield, H. 1969, ApJ, 156, L27
Zinnecker, H., & Yorke, H. W. 2007, ARA&A, 45, 481

Appendix A: Supplementary materials

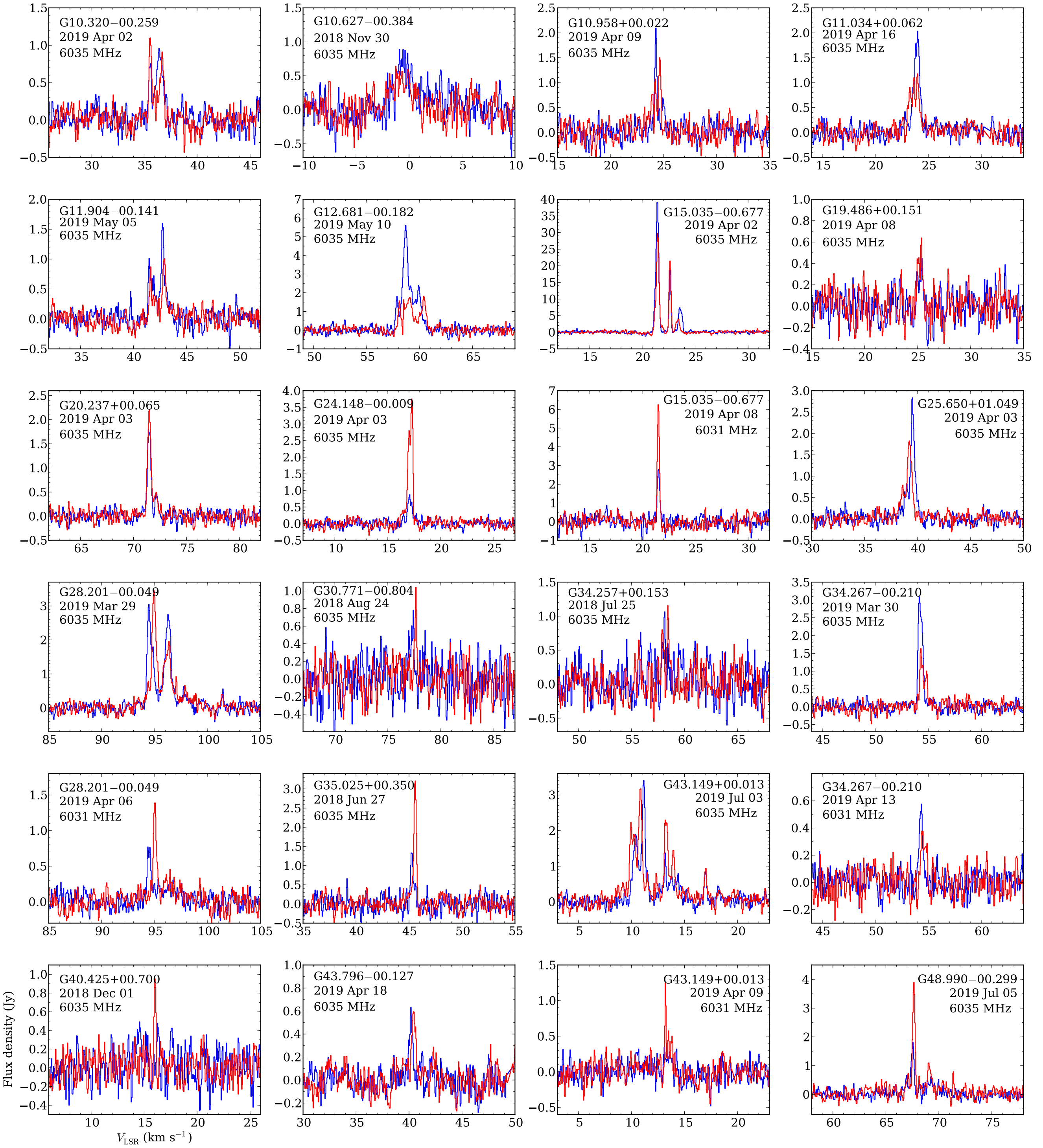

Fig. A.1. 6035 and 6031 MHz OH maser spectra as detected in the Torun survey. Red and blue lines are RHC and LHC polarisations, respectively.

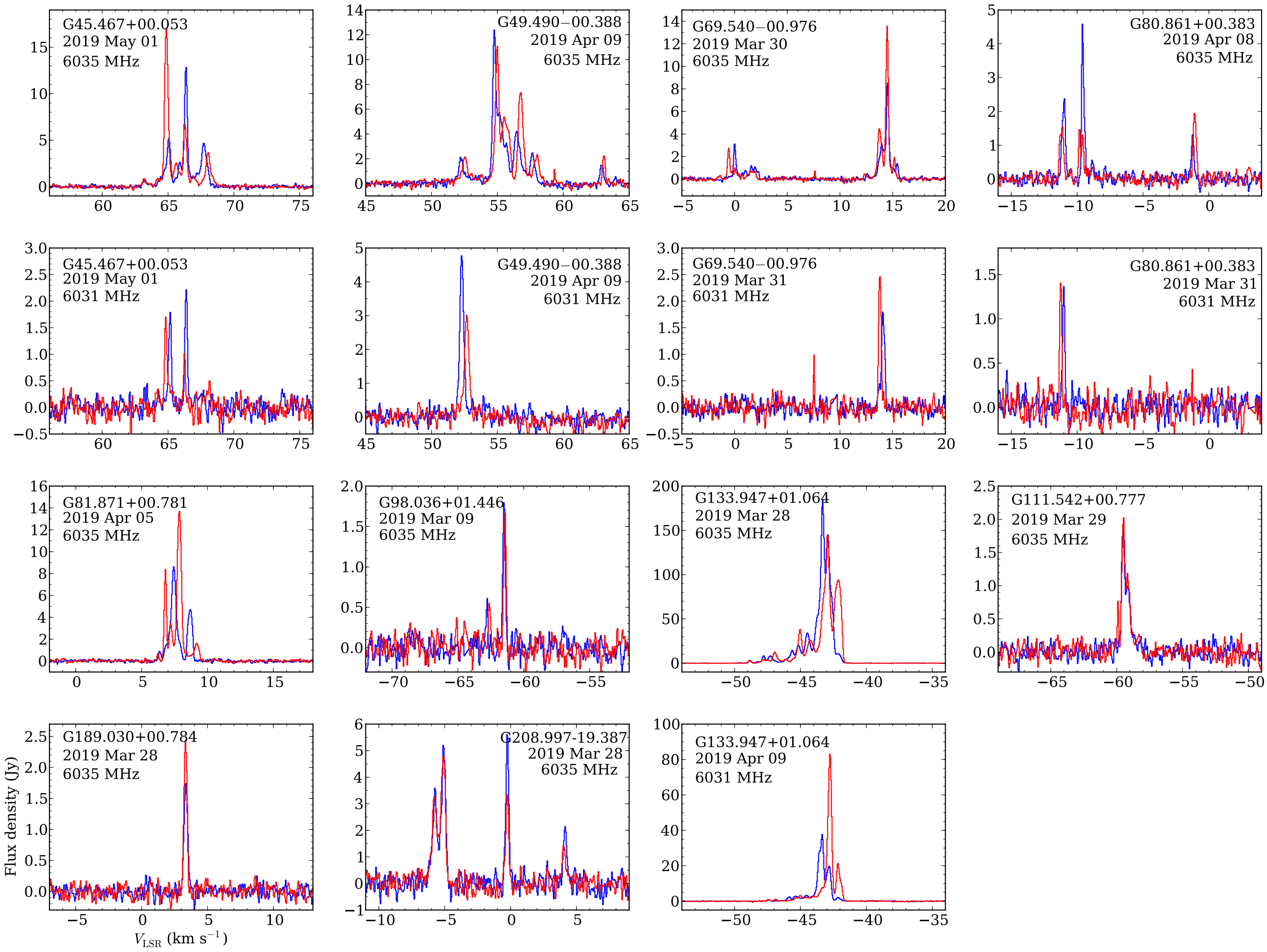

Fig. A.1. continued.

Table A.1. Properties of 6035 and 6031 MHz OH maser emission for previously known sources.

Name (l b)	RA (J2000)	Dec (J2000)	ΔV	LHC			RHC		
				V_p	S_p	S_i	V_p	S_p	S_i
(° °)	(h m s)	(° ′ ″)	(km s^{-1})	(km s^{-1})	(Jy)	(Jy km s^{-1})	(km s^{-1})	(Jy)	(Jy km s^{-1})
G10.320–00.259	18 09 23.30	−20 08 06.90	35.3;37.2	36.41	0.96	0.97	35.59	1.10	0.69
G10.627–00.384	18 10 29.22	−19 55 41.10	−2.2;1.1	−0.91	0.89	2.02	−1.24	0.64	1.20
G10.958+00.022	18 09 39.32	−19 26 28.00	23.8;25.3	24.32	2.10	0.77	24.66	1.50	0.70
G11.034+00.062	18 09 39.84	−19 21 20.30	23.0;24.5	23.99	2.03	1.27	23.99	1.18	0.94
G11.904–00.141	18 12 11.44	−18 41 28.60	41.3;43.7	42.74	1.60	1.28	42.94	1.01	0.88
G12.681–00.182	18 13 54.75	−18 01 46.60	57.6;60.8	58.69	5.59	5.83	60.39	1.82	2.91
G15.035–00.677	18 20 24.78	−16 11 34.60	21.0;23.9	21.42	39.04	20.48	21.46	29.81	16.34
	6031		21.3;21.8	21.51	6.25	1.49	21.56	2.78	0.74
G19.486+00.151	18 26 00.39	−11 52 22.60	24.7,25.7	25.40	0.45	0.19	25.35	0.64	0.25
G20.237+00.065	18 27 44.56	−11 14 54.30	71.07;72.5	71.42	1.79	0.83	71.51	2.20	1.03
G24.148–00.009	18 35 20.94	−07 48 55.67	16.3;17.7	17.06	0.87	0.35	17.25	3.75	1.73
G25.650+01.049	18 34 20.90	−05 59 42.20	38.1;40.2	39.52	2.84	0.16	39.23	1.83	1.28
G28.201−00.049	18 42 58.08	−04 13 56.20	94.0;98.9	94.46	3.05	4.20	94.94	3.45	4.04
	6031		94.3;97.6	94.30	0.77	0.76	95.04	1.39	0.95
G30.771−00.804	18 50 21.55	−02 17 24.00	76.8,77.9	77.41	0.78	0.27	77.65	1.04	0.20
G34.257+00.153	18 53 18.63	+01 14 57.40	57.5;58.7	58.14	1.06	0.25	58.43	1.15	0.50
G34.267–00.210	18 54 37.25	+01 05 33.70	53.9;55.0	54.16	3.09	1.47	54.31	1.64	0.82
	6031		53.9;54.8	54.35	0.58	0.23	54.40	0.38	0.16
G35.025+00.350	18 54 00.66	+02 01 19.30	45.1;45.7	45.21	1.33	0.45	45.60	3.21	0.85
G40.425+00.700	19 02 39.62	06 59 10.50	15.8;16.1	–	–	0.05	16.03	0.95	0.15
G43.149+00.013	19 10 11.05	+09 05 20.40	8.5;18.6	11.15	3.41	3.95	10.86	3.17	5.67
	6031		12.9;14.0	–	–	0.16	13.19	1.25	0.37
G43.796–00.127	19 11 53.97	+09 35 53.50	39.8;40.7	40.18	0.63	0.22	40.43	0.60	0.35
G45.467+00.053	19 14 24.15	+11 09 43.00	62.7;68.6	66.38	12.82	10.63	64.87	17.06	12.16
	6031		63.9;68.3	66.38	2.22	1.03	64.83	1.70	0.94
G48.990–00.299	19 22 26.13	+14 06 39.78	66.7;69.6	67.55	1.81	1.34	67.65	3.89	1.96
G49.490–00.388	19 23 43.95	+14 30 34.20	52.1;63.3	54.76	12.39	13.25	55.00	11.07	14.80
	6031		52.1;53.1	52.28	4.77	1.93	52.67	3.01	1.40
G69.540–00.976	20 10 09.07	+31 31 34.86	−0.9;15.7	14.53	8.52	7.53	14.48	13.56	8.69
	6031		13.4;14.3	14.05	1.80	0.69	13.81	2.46	0.73
G80.861+00.383	20 37 00.96	+41 34 55.70	−11.5;−0.8	−9.60	4.58	2.45	−1.10	1.94	1.70
	6031		−11.2;−10.7	−11.01	1.37	0.28	−11.26	1.40	0.19
G81.871+00.781	20 38 36.42	+42 37 34.56	6.1;9.5	7.44	8.63	7.09	7.87	13.68	9.34
G98.036+01.446	21 43 01.43	+54 56 17.75	−63.0;−61.3	−62.76	0.61	0.49	−62.60	0.55	0.49
G111.542+00.777	23 13 45.36	+61 28 10.55	−60.4;−58.1	−59.52	1.91	0.92	−59.47	2.02	1.18
G133.947+01.064	02 27 03.82	+61 02 25.4	−49.1;−41.1	−43.31	184.16	190.1	−42.92	144.04	181.9
	6031		−47.7;−41.4	−43.35	37.72	30.84	−42.77	83.04	45.85
G189.030+00.784	06 08 40.67	+21 31 06.90	3.0;3.7	3.37	1.74	0.57	3.32	2.43	0.70
G208.997–19.387	05 35 14.50	−05 22 45.00	−6.4;4.6	−0.27	5.60	5.92	−5.07	4.80	4.42

Notes. The following parameters are listed; velocity range of I Stokes emission (ΔV), peak velocity (V_p), peak flux density (S_p), and integrated flux density (S_i) for the LHC and RHC polarisations.

Table A.2. Non-detections.

Name (l b) (° °)	RA (J200) (h m s)	Dec (J2000) (° ′ ″)	V_c(6668) ($km\,s^{-1}$)	Ref.
G08.317−00.096	18 04 36.02	21 48 19.60	46.9	
G08.669−00.356	18 06 18.99	−21 37 32.20	39.2	1
G08.683−00.368	18 06 23.49	−21 37 10.20	43.1	
G08.832−00.028	18 05 25.66	−21 19 25.50	−3.9	
G08.872−00.493	18 07 15.32	−21 30 54.40	23.2	
G09.215−00.202	18 06 52.84	−21 04 27.50	45.5	
G09.621+00.196	18 06 14.67	−20 31 32.40	1.2	2
G09.619+00.193	18 06 14.92	−20 31 44.30	5.5	2
G09.986−00.028	18 07 50.12	−20 18 56.50	42.2	
G10.205−00.345	18 09 28.43	−20 16 42.50	6.6	
G10.287−00.125	18 08 49.36	−20 05 59.00	4.6	
G10.299−00.146	18 08 55.54	−20 05 57.50	19.9	
G10.323−00.160	18 09 01.46	−20 05 07.80	11.5	
G10.342−00.142	18 08 59.99	−20 03 35.40	15.4	
G10.356−00.148	18 09 03.07	−20 03 02.20	49.9	
G10.444−00.018	18 08 44.88	−19 54 38.20	73.3	
G10.472+00.027	18 08 38.20	−19 51 50.10	75.0	
G10.480+00.033	18 08 37.88	−19 51 16.10	59.5	
G10.629−00.333	18 10 17.98	−19 54 04.80	−8.1	
G10.724−00.334	18 10 30.03	−19 49 06.80	−2.2	
G10.822−00.103	18 09 50.52	−19 37 14.10	72.0	
G10.886+00.123	18 09 07.98	−19 27 21.80	17.1	
G11.109−00.114	18 10 28.25	−19 22 29.10	23.9	
G11.497−01.485	18 16 22.13	−19 41 27.10	6.6	
G11.903−00.102	18 12 02.70	−18 40 24.70	33.9	
G11.936−00.150	18 12 17.29	−18 40 02.60	48.5	
G11.936−00.616	18 14 00.89	−18 53 26.60	32.2	
G11.992−00.272	18 12 51.19	−18 40 38.40	59.8	
G12.025−00.031	18 12 01.86	−18 31 55.70	108.2	
G12.112−00.126	18 12 33.39	−18 30 07.60	39.9	
G12.181−00.123	18 12 41.00	−18 26 21.90	29.7	
G12.199−00.034	18 12 23.44	−18 22 50.90	49.3	
G12.202−00.120	18 12 42.93	−18 25 11.80	26.4	
G12.203−00.107	18 12 40.24	−18 24 47.50	20.5	
G12.265−00.051	18 12 35.40	−18 19 52.30	68.3	
G12.526+00.016	18 12 52.04	−18 04 13.60	42.6	
G12.625−00.017	18 13 11.30	−17 59 57.60	21.5	
G12.776+00.128	18 12 57.57	−17 47 49.20	32.8	
G12.889+00.489	18 11 51.40	−17 31 29.60	39.2	
G12.904−00.031	18 13 48.27	−17 45 38.80	58.8	
G12.909−00.260	18 14 39.53	−17 52 00.00	39.8	
G13.179+00.061	18 14 00.96	−17 28 32.50	46.4	
G13.657−00.599	18 17 24.27	−17 22 12.50	51.1	
G13.696−00.156	18 15 51.05	−17 07 29.60	99.3	
G13.713−00.083	18 15 36.99	−17 04 31.80	43.5	
G14.101+00.087	18 15 45.80	−16 39 09.70	15.3	
G14.230−00.509	18 18 12.59	−16 49 22.80	25.3	
G14.331−00.641	18 18 53.80	−16 47 46.60	22.6	
G14.390−00.020	18 16 43.77	−16 27 01.00	26.9	
G14.457−00.143	18 17 18.79	−16 27 57.50	43.2	
G14.490+00.014	18 16 48.06	−16 20 45.00	20.2	
G14.521+00.155	18 16 20.73	−16 15 05.50	4.1	
G14.604+00.017	18 17 01.14	−16 14 38.00	24.6	
G14.631−00.577	18 19 15.21	−16 30 04.50	25.2	
G14.991−00.121	18 18 17.32	−15 58 08.30	46.0	
G15.094+00.192	18 17 20.82	−15 43 46.50	25.7	
G15.607−00.255	18 19 59.34	−15 29 22.80	65.9	
G15.665−00.499	18 20 59.75	−15 33 10.00	−3.0	
G16.112−00.303	18 21 09.14	−15 04 00.60	34.5	
G16.302−00.196	18 21 07.83	−14 50 54.60	51.8	
G16.403−00.181	18 21 16.39	−14 45 09.00	39.2	
G16.585−00.051	18 21 09.13	−14 31 48.50	62.1	
G16.662−00.331	18 22 19.46	−14 35 39.10	43.0	
G16.831+00.079	18 21 09.53	−14 15 08.60	58.7	
G16.855+00.641	18 19 09.57	−13 57 57.50	24.2	
G16.864−02.159	18 29 24.42	−15 16 04.50	14.9	
G16.976−00.005	18 21 44.68	−14 09 48.50	6.5	
G17.021−02.403	18 30 36.30	−15 14 28.50	23.5	
G17.029−00.071	18 22 05.21	−14 08 51.00	91.3	
G17.638+00.157	18 22 26.30	−13 30 12.10	20.7	
G17.862+00.074	18 23 10.10	−13 20 40.80	110.6	
G18.073+00.077	18 23 33.98	−13 09 25.00	55.5	
G18.159+00.094	18 23 40.18	−13 04 21.00	58.3	
G18.262−00.244	18 25 05.70	−13 08 23.20	75.7	
G18.341+01.768	18 17 58.13	−12 07 24.80	28.0	
G18.440+00.045	18 24 23.32	−12 50 52.10	61.8	
G18.460−00.004	18 24 36.34	−12 51 08.60	49.4	2
G18.661+00.034	18 24 51.10	−12 39 22.50	79.0	
G18.667+00.025	18 24 53.78	−12 39 20.80	78.7	
G18.733−00.224	18 25 55.53	−12 42 48.90	45.8	
G18.735−00.227	18 25 56.46	−12 42 50.00	37.9	
G18.834−00.300	18 26 23.66	−12 39 38.00	41.1	2
G18.874+00.053	18 25 11.34	−12 27 36.80	38.6	
G18.888−00.475	18 27 07.85	−12 41 35.90	56.5	
G18.999−00.239	18 26 29.24	−12 29 07.10	69.4	
G19.009−00.029	18 25 44.77	−12 22 46.00	55.2	
G19.249+00.267	18 25 08.02	−12 01 42.20	20.4	
G19.267+00.349	18 24 52.38	−11 58 28.20	16.2	
G19.365−00.030	18 26 25.78	−12 03 53.30	25.2	
G19.472+00.170	18 25 54.70	−11 52 34.60	21.6	
G19.496+00.115	18 26 09.16	−11 52 51.70	121.1	
G19.609−00.234	18 27 37.99	−11 56 37.60	40.2	
G19.612−00.120	18 27 13.48	−11 53 15.70	53.1	
G19.612−00.134	18 27 16.52	−11 53 38.20	56.5	
G19.614+00.011	18 26 45.24	−11 49 31.40	32.8	
G19.667+00.114	18 26 28.97	−11 43 48.90	14.2	
G19.701−00.267	18 27 55.52	−11 52 40.30	43.8	
G19.755−00.128	18 27 31.66	−11 45 55.00	123.0	2
G19.884−00.534	18 29 14.37	−11 50 23.00	46.7	
G20.081−00.135	18 28 10.32	−11 28 47.60	43.5	
G20.364−00.013	18 28 15.91	−11 10 20.40	55.9	
G20.733−00.059	18 29 07.99	−10 52 00.60	60.7	
G20.926−00.050	18 29 27.79	−10 41 28.80	27.4	
G20.963−00.075	18 29 37.34	−10 40 12.60	34.6	

Notes. The central velocity V_c of observation is given. Previously known sources are bolded and reference for detection is given in the last column.

References. (1) Caswell & Vaile (1995); (2) Avison et al. (2016); (3) Baudry et al. (1997).

Table A.2. continued.

Name (l b) (° °)	RA (J200) (h m s)	Dec (J2000) (° ′ ″)	V_c(6668) (km s^{-1})	Ref.
G21.023−00.063	18 29 41.55	−10 36 42.30	31.1	
G21.407−00.254	18 31 06.33	−10 21 37.41	88.9	
G21.563−00.033	18 30 36.07	−10 07 10.90	117.2	
G21.848−00.240	18 31 53.06	−09 57 45.40	81.9	
G21.880+00.014	18 31 01.75	−09 49 00.50	20.3	
G22.039+00.222	18 30 34.70	−09 34 47.00	53.2	
G22.335−00.155	18 32 29.40	−09 29 29.68	35.6	
G22.357+00.066	18 31 44.12	−09 22 12.31	80.1	
G22.435−00.169	18 32 43.82	−09 24 33.20	29.5	1
G23.003+00.124	18 32 44.25	−08 46 10.70	110.5	
G23.010−00.411	18 34 40.29	−09 00 38.10	74.7	
G23.126+00.395	18 31 59.75	−08 32 09.10	13.8	
G23.207−00.377	18 34 55.21	−08 49 14.89	81.6	
G23.257−00.241	18 34 31.26	−08 42 46.70	63.9	
G23.365−00.291	18 34 54.13	−08 38 25.60	82.5	
G23.389+00.185	18 33 14.32	−08 23 57.47	75.3	
G23.437−00.184	18 34 39.25	−08 31 38.50	102.9	
G23.440−00.182	18 34 39.18	−08 31 25.40	96.6	
G23.484+00.097	18 33 44.05	−08 21 20.60	87.0	
G23.657−00.127	18 34 51.56	−08 18 21.30	82.4	
G23.707−00.198	18 35 12.36	−08 17 39.36	76.4	
G23.818+00.384	18 33 19.50	−07 55 38.10	76.2	
G23.885+00.060	18 34 36.84	−08 01 00.70	45.0	
G23.901+00.077	18 34 34.92	−07 59 42.20	35.7	
G23.966−00.109	18 35 22.21	−08 01 22.47	70.8	
G23.986−00.089	18 35 20.09	−07 59 45.00	65.1	
G23.996−00.100	18 35 23.49	−07 59 29.80	68.2	
G24.329+00.144	18 35 08.14	−07 35 04.00	110.3	
G24.461+00.198	18 35 11.33	−07 26 31.10	125.5	
G24.493−00.039	18 36 05.83	−07 31 20.60	115.0	
G24.541+00.312	18 34 55.72	−07 19 06.65	105.5	
G24.631+00.172	18 35 35.77	−07 18 08.75	115.9	
G24.634−00.324	18 37 22.71	−07 31 42.14	35.5	
G24.676−00.150	18 36 49.97	−07 24 42.10	116.1	
G24.790+00.083	18 36 12.56	−07 12 10.79	113.3	
G24.791+00.082	18 36 13.13	−07 12 08.20	105.8	
G24.850+00.087	18 36 18.40	−07 08 51.00	110.0	
G24.920+00.088	18 36 25.94	−07 05 07.80	53.3	
G24.943+00.074	18 36 31.55	−07 04 16.80	53.2	
G25.226+00.288	18 36 16.97	−06 43 18.30	42.0	
G25.270−00.434	18 38 56.96	−07 00 49.20	65.9	
G25.382−00.182	18 38 15.20	−06 47 56.20	58.2	
G25.395+00.034	18 37 30.28	−06 41 17.70	95.4	
G25.407−00.170	18 38 15.52	−06 46 16.70	60.8	
G25.411+00.105	18 37 16.92	−06 38 30.50	97.2	
G25.494+00.062	18 37 35.44	−06 35 13.40	103.8	
G25.613+00.226	18 37 13.42	−06 24 24.20	110.1	
G25.826−00.178	18 39 03.63	−06 24 09.70	91.7	
G25.838−00.378	18 39 47.88	−06 29 00.90	−1.6	
G25.920−00.141	18 39 06.07	−06 18 04.70	114.8	
G26.422+01.685	18 33 30.51	−05 01 02.00	31.0	
G26.545+00.423	18 38 14.46	−05 29 16.80	82.5	
G26.527−00.267	18 40 40.26	−05 49 12.90	104.2	
G26.552−00.309	18 40 52.03	−05 49 02.56	105.3	
G26.598−00.024	18 39 55.92	−05 38 44.64	24.8	
G26.601−00.221	18 40 38.57	−05 44 01.60	103.4	
G26.648+00.018	18 39 52.68	−05 34 54.60	109.4	
G27.011−00.039	18 40 44.88	−05 17 09.80	−18.3	
G27.221+00.136	18 40 30.54	−05 01 05.39	118.8	
G27.286+00.151	18 40 34.51	−04 57 14.40	34.8	
G27.365−00.166	18 41 51.06	−05 01 43.50	99.8	
G27.500+00.107	18 41 07.38	−04 47 02.30	87.3	
G27.757+00.050	18 41 47.99	−04 34 52.60	99.2	
G27.783−00.259	18 42 56.96	−04 41 59.00	98.3	
G27.784+00.057	18 41 49.58	−04 33 13.80	111.9	
G27.869−00.235	18 43 01.55	−04 36 43.10	20.1	
G28.011−00.426	18 43 57.96	−04 34 21.90	16.9	
G28.226+00.359	18 41 33.57	−04 01 22.34	49.7	
G28.282−00.359	18 44 13.26	−04 18 04.80	41.3	
G28.321−00.011	18 43 03.11	−04 06 26.40	104.8	
G28.397+00.081	18 42 51.98	−03 59 53.60	71.5	
G28.523+00.127	18 42 55.89	−03 51 55.40	39.6	
G28.532+00.129	18 42 56.50	−03 51 21.60	27.0	
G28.608+00.018	18 43 28.52	−03 50 22.80	106.4	
G28.687−00.283	18 44 41.54	−03 54 22.10	92.3	
G28.700+00.406	18 42 15.57	−03 34 46.90	94.2	
G28.817+00.365	18 42 37.34	−03 29 40.92	90.7	2
G28.832−00.253	18 44 51.08	−03 45 48.50	91.8	
G28.842+00.493	18 42 12.54	−03 24 51.10	83.2	
G28.848−00.228	18 44 47.46	−03 44 17.20	102.8	
G28.861+00.065	18 43 46.24	−03 35 33.40	105.3	
G28.929+00.019	18 44 03.56	−03 33 11.83	47.1	
G29.282−00.330	18 45 56.96	−03 23 56.54	92.1	
G29.320−00.162	18 45 25.16	−03 17 16.90	48.9	
G29.581+00.133	18 44 50.92	−02 55 15.92	31.7	
G29.603−00.625	18 47 35.41	−03 14 50.10	80.5	
G29.724+00.107	18 45 11.97	−02 48 21.59	95.8	
G29.863−00.044	18 45 59.57	−02 45 04.40	101.4	
G29.915−00.023	18 46 00.94	−02 41 42.26	103.0	
G29.955−00.016	18 46 03.74	−02 39 22.20	96.0	
G29.961−00.067	18 46 15.36	−02 40 28.81	100.5	
G29.978−00.047	18 46 12.96	−02 39 01.40	96.9	
G29.993−00.282	18 47 04.82	−02 44 39.80	103.2	
G30.010−00.273	18 47 04.71	−02 43 31.20	106.1	
G30.198−00.169	18 47 03.04	−02 30 36.40	108.2	
G30.225−00.180	18 47 08.30	−02 29 28.90	113.2	
G30.317+00.070	18 46 25.02	−02 17 40.75	36.1	
G30.370+00.482	18 45 02.72	−02 03 33.70	12.4	
G30.400−00.296	18 47 52.30	−02 23 16.05	98.2	
G30.419−00.232	18 47 40.76	−02 20 30.10	102.9	
G30.423+00.466	18 45 12.08	−02 01 13.60	7.5	
G30.542+00.011	18 47 02.26	−02 07 17.70	53.1	
G30.582−00.141	18 47 39.20	−02 09 19.00	115.5	
G30.589−00.043	18 47 18.86	−02 06 17.20	43.0	
G30.622+00.082	18 46 55.78	−02 01 07.18	39.6	
G30.703−00.068	18 47 36.82	−02 00 53.80	88.2	

Table A.2. continued.

Name (l b) (° °)	RA (J200) (h m s)	Dec (J2000) (° ′ ″)	V_c(6668) (km s^{-1})	Ref.
G30.760−00.052	18 47 39.78	−01 57 23.40	91.7	
G30.774+00.078	18 47 13.42	−01 53 04.15	98.5	
G30.780+00.230	18 46 41.52	−01 48 37.10	48.9	
G30.788+00.204	18 46 48.09	−01 48 53.90	84.5	
G30.818−00.057	18 47 46.97	−01 54 26.40	101.3	
G30.822−00.053	18 47 46.53	−01 54 07.40	93.2	
G30.851+00.123	18 47 12.26	−01 47 46.60	27.5	
G30.898+00.161	18 47 09.13	−01 44 11.10	101.8	
G30.960+00.086	18 47 32.00	−01 42 57.60	40.1	
G30.963+00.225	18 47 02.62	−01 38 58.34	102.2	
G30.972−00.142	18 48 22.07	−01 48 30.30	77.8	
G30.973+00.562	18 45 51.69	−01 29 13.30	19.9	
G30.980+00.216	18 47 06.47	−01 38 20.00	111.0	
G31.047+00.356	18 46 43.85	−01 30 54.15	81.1	
G31.059+00.093	18 47 41.35	−01 37 26.20	16.5	
G31.076+00.457	18 46 25.44	−01 26 33.50	25.5	
G31.122+00.063	18 47 54.68	−01 34 56.90	48.0	
G31.158+00.046	18 48 02.40	−01 33 26.80	41.1	
G31.182−00.148	18 48 46.41	−01 37 28.10	46.3	
G31.253+00.003	18 48 21.92	−01 29 35.68	41.2	
G31.276+00.006	18 48 23.79	−01 28 17.88	37.2	
G31.281+00.061	18 48 12.43	−01 26 30.10	110.3	
G31.395−00.258	18 49 33.09	−01 29 06.93	87.4	
G31.412+00.307	18 47 34.29	−01 12 45.60	95.8	
G31.581+00.077	18 48 41.94	−01 10 02.53	98.8	
G31.975+00.180	18 49 03.05	−00 46 11.12	92.4	
G32.045+00.059	18 49 36.56	−00 45 45.90	92.8	
G32.082+00.078	18 49 36.60	−00 43 16.40	92.9	
G32.105−00.074	18 50 11.58	−00 46 12.32	49.7	
G32.117+00.091	18 49 37.70	−00 41 00.93	92.6	
G32.516+00.323	18 49 31.74	−00 13 20.80	52.5	
G32.704−00.056	18 51 13.22	−00 13 42.31	40.6	
G32.744−00.075	18 51 21.87	−00 12 05.00	38.5	2
G32.802+00.193	18 50 30.98	−00 01 39.00	27.2	
G32.821−00.330	18 52 24.76	−00 14 56.87	82.1	
G32.825−00.328	18 52 24.69	−00 14 39.70	82.4	
G32.914−00.096	18 51 44.69	−00 03 35.50	103.5	
G32.917−00.094	18 51 44.74	−00 03 20.16	103.2	
G32.963−00.340	18 52 42.35	−00 07 39.10	46.7	
G32.965−00.340	18 52 42.39	−00 07 32.97	48.1	
G32.992+00.034	18 51 25.58	00 04 08.33	91.9	
G33.093−00.073	18 51 59.58	00 06 35.50	103.9	
G33.133−00.092	18 52 07.82	00 08 12.80	73.2	
G33.199+00.001	18 51 55.34	00 14 19.38	91.2	
G33.204−00.010	18 51 58.14	00 14 13.61	91.9	
G33.317−00.360	18 53 25.30	00 10 43.90	28.1	
G33.393+00.010	18 52 14.62	00 24 52.90	105.2	
G33.424−00.315	18 53 27.40	00 17 40.64	45.6	
G33.486+00.040	18 52 18.39	00 30 40.20	121.7	
G33.641−00.228	18 53 32.56	00 31 39.18	60.3	
G33.634−00.021	18 52 47.56	00 36 54.20	103.1	
G33.725−00.120	18 53 18.78	00 39 05.00	54.1	
G33.852+00.018	18 53 03.09	00 49 36.50	61.0	

Table A.2. continued.

Name (l b) (° °)	RA (J200) (h m s)	Dec (J2000) (° ′ ″)	V_c(6668) (km s^{-1})	Ref.
G33.980−00.019	18 53 25.01	00 55 25.98	59.0	
G34.096+00.018	18 53 29.94	01 02 39.40	56.1	
G34.195−00.593	18 55 51.30	00 51 13.58	61.7	
G34.244+00.133	18 53 21.44	01 13 44.40	54.9	
G34.284+00.184	18 53 15.00	01 17 12.99	51.8	
G34.396+00.222	18 53 19.08	01 24 13.80	55.7	
G34.411+00.235	18 53 17.99	01 25 25.26	63.1	
G34.751−00.093	18 55 05.22	01 34 36.26	52.9	
G34.757+00.025	18 54 40.74	01 38 06.40	76.5	
G34.791−01.387	18 59 45.98	01 01 19.00	46.9	
G34.822+00.352	18 53 37.84	01 50 33.00	59.6	
G35.132−00.744	18 58 06.14	01 37 07.50	35.4	2
G35.149+00.809	18 52 35.96	02 20 32.03	75.2	
G35.197−00.743	18 58 13.05	01 40 35.70	28.5	2
G35.200−01.736	19 01 45.54	01 13 32.60	44.5	1
G35.226−00.354	18 56 53.15	01 52 46.89	59.3	
G35.247−00.237	18 56 30.38	01 57 08.88	72.4	
G35.397+00.025	18 55 50.78	02 12 19.10	89.2	
G35.417−00.284	18 56 59.02	02 04 55.65	56.0	
G35.457−00.179	18 56 40.98	02 09 57.16	55.5	
G35.588+00.060	18 56 04.22	02 23 28.30	44.1	
G35.793−00.175	18 57 16.89	02 27 57.91	60.7	
G36.115+00.552	18 55 16.79	03 05 05.41	73.1	
G36.634−00.203	18 58 55.23	03 12 04.72	77.3	
G36.705+00.096	18 57 59.12	03 24 06.11	53.0	
G36.839−00.022	18 58 39.21	03 28 00.90	61.6	
G36.918+00.483	18 56 59.78	03 46 03.60	−35.8	
G37.030−00.039	18 59 03.64	03 37 45.09	80.2	
G37.043−00.035	18 59 04.41	03 38 32.80	80.2	
G37.430+01.518	18 54 14.23	04 41 41.10	41.2	
G37.479−00.105	19 00 07.14	03 59 53.35	54.7	
G37.546−00.112	19 00 16.05	04 03 16.09	49.9	
G37.554+00.201	18 59 09.98	04 12 15.54	83.6	
G37.598+00.425	18 58 26.79	04 20 45.46	87.0	
G37.735−00.112	19 00 36.84	04 13 20.00	50.3	
G37.753−00.189	19 00 55.42	04 12 12.56	54.6	
G37.767−00.214	19 01 02.27	04 12 16.60	69.0	
G38.038−00.300	19 01 50.46	04 24 18.96	58.1	
G38.119−00.229	19 01 44.15	04 30 37.42	70.4	
G38.203−00.067	19 01 18.73	04 39 34.29	84.2	
G38.255−00.200	19 01 52.95	04 38 39.47	73.1	
G38.258−00.073	19 01 26.25	04 42 19.90	15.4	
G38.565+00.538	18 59 49.13	05 15 28.90	−28.8	
G38.598−00.212	19 02 33.46	04 56 36.40	62.5	
G38.653+00.088	19 01 35.24	05 07 47.36	−31.5	
G38.916−00.353	19 03 38.65	05 09 42.49	31.9	
G39.100+00.491	19 00 58.04	05 42 43.90	15.9	
G39.388−00.141	19 03 45.31	05 40 42.68	60.2	
G40.282−00.219	19 05 41.21	06 26 12.69	73.9	2
G40.597−00.719	19 08 03.29	06 29 12.90	76.2	
G40.623−00.138	19 06 01.63	06 46 36.50	31.1	1
G41.075−00.125	19 06 49.04	07 11 06.57	57.5	
G41.121−00.107	19 06 50.24	07 14 01.49	36.6	

Table A.2. continued.

Name (l b) (° °)	RA (J200) (h m s)	Dec (J2000) (° ′ ″)	V_c(6668) (km s^{-1})	Ref.
G41.123−00.220	19 07 14.85	07 11 00.69	63.4	
G41.156−00.201	19 07 14.37	07 13 18.10	56.0	
G41.226−00.197	19 07 21.37	07 17 08.17	55.4	
G41.347−00.136	19 07 21.84	07 25 17.27	11.8	
G42.034+00.190	19 07 28.18	08 10 53.47	12.8	
G42.133+00.517	19 06 28.90	08 25 10.00	−33.3	
G42.303−00.299	19 09 43.59	08 11 41.41	28.1	
G42.435−00.260	19 09 49.85	08 19 45.40	66.7	
G42.698−00.147	19 09 55.06	08 36 53.45	−42.9	
G43.038−00.453	19 11 38.98	08 46 30.71	54.8	
G43.074−00.077	19 10 22.05	08 58 51.49	10.2	
G43.180−00.518	19 12 09.02	08 52 14.30	58.9	
G43.890−00.784	19 14 26.39	09 22 36.50	47.6	
G44.310+00.041	19 12 15.81	10 07 53.52	56.0	
G44.644−00.516	19 14 53.76	10 10 07.69	49.5	
G45.071+00.132	19 13 22.12	10 50 53.11	57.7	
G45.380−00.594	19 16 34.14	10 47 01.60	53.3	
G45.445+00.069	19 14 18.31	11 08 59.40	50.0	
G45.473+00.134	19 14 07.36	11 12 16.00	65.7	
G45.493+00.126	19 14 11.35	11 13 06.20	57.2	
G45.804−00.356	19 16 31.08	11 16 12.01	59.9	
G46.066+00.220	19 14 56.07	11 46 12.98	23.5	
G46.115+00.387	19 14 25.52	11 53 25.99	58.2	
G48.902−00.273	19 22 10.33	14 02 43.51	71.8	
G49.043−01.079	19 25 22.25	13 47 19.50	36.6	
G49.265+00.311	19 20 44.85	14 38 26.91	−4.7	
G49.349+00.413	19 20 32.44	14 45 45.44	67.9	
G49.416+00.326	19 20 59.21	14 46 49.60	−12.1	
G49.417+00.324	19 20 59.82	14 46 49.10	−26.6	
G49.470−00.371	19 23 37.90	14 29 59.30	63.8	
G49.471−00.369	19 23 37.60	14 30 05.40	73.5	
G49.482−00.402	19 23 46.19	14 29 47.10	51.8	
G49.489−00.369	19 23 39.82	14 31 04.90	56.2	
G49.599−00.249	19 23 26.61	14 40 16.99	63.0	
G49.617−00.360	19 23 52.81	14 38 03.30	50.4	
G50.035+00.582	19 21 15.45	15 26 49.20	−5.1	
G50.315+00.676	19 21 27.47	15 44 18.60	30.1	
G50.779+00.152	19 24 17.41	15 54 01.60	49.1	
G51.679+00.719	19 23 58.87	16 57 41.80	7.3	
G51.818+01.250	19 22 17.95	17 20 06.50	46.5	
G52.199+00.723	19 24 59.84	17 25 17.90	3.7	
G52.663−01.092	19 32 36.07	16 57 38.40	65.8	
G52.922+00.414	19 27 34.96	17 54 38.14	39.1	
G53.036+00.113	19 28 55.49	17 52 03.11	10.0	
G53.142+00.071	19 29 17.58	17 56 23.21	24.6	
G53.618+00.036	19 30 23.01	18 20 26.68	18.9	
G56.963−00.235	19 38 17.10	21 08 05.40	29.9	
G57.610+00.025	19 38 40.74	21 49 32.70	38.9	
G58.775+00.644	19 38 49.13	23 08 40.20	33.3	
G59.634−00.192	19 43 50.00	23 28 38.80	29.6	
G59.783+00.065	19 43 11.25	23 44 03.30	27.0	
G59.833+00.672	19 40 59.33	24 04 46.50	38.0	

Table A.2. continued.

Name (l b) (° °)	RA (J200) (h m s)	Dec (J2000) (° ′ ″)	V_c(6668) (km s^{-1})	Ref.
G60.575+00.186	19 45 52.48	24 17 42.99	3.4	
G70.181+01.741	20 00 54.16	33 31 30.88	−26.8	
G71.522+00.385	20 12 57.91	33 30 26.95	8.2	
G73.063+01.796	20 08 10.20	35 59 23.70	5.9	
G75.782+00.342	20 21 44.05	37 26 36.91	−1.0	
G78.122+03.633	20 14 26.04	41 13 33.39	−7.7	
G78.886+00.708	20 29 24.94	40 11 19.28	−6.9	
G79.736+00.991	20 30 50.67	41 02 27.60	−5.5	
G81.722+00.571	20 39 01.05	42 22 49.18	−2.7	3
G81.744+00.590	20 39 00.38	42 24 36.91	4.0	
G81.752+00.590	20 39 01.99	42 24 59.08	−5.7	
G81.871+00.780	20 38 36.42	42 37 34.56	6.3	
G94.602−01.796	21 39 58.26	50 14 20.96	−40.8	
G97.521+03.172	21 32 13.00	55 52 56.00	−71.2	
G107.288+05.638	22 21 22.50	63 51 13.00	−8.5	
G108.184+05.519	22 28 51.40	64 13 41.31	−11.0	
G108.766−00.986	22 58 51.18	58 45 14.37	−46.3	
G109.871+02.114	22 56 17.90	62 01 49.65	−3.7	3
G111.255−00.769	23 16 10.33	59 55 28.43	−38.9	
G121.298+00.659	00 36 47.35	63 29 02.16	−23.3	
G123.066−06.309	00 52 24.19	56 33 43.17	−29.4	
G136.845+01.167	02 49 33.59	60 48 27.95	−45.0	
G173.482+02.446	05 39 13.05	35 45 51.29	−13.0	
G173.698+02.886	05 41 37.40	35 48 49.00	−23.8	
G174.201−00.071	05 30 48.01	33 47 54.61	1.5	
G188.793+01.030	06 09 06.96	21 50 41.23	−5.3	
G188.946+00.886	06 08 53.34	21 38 29.16	10.8	
G189.471−01.216	06 02 08.37	20 09 20.10	18.8	
G189.777+00.344	06 08 35.30	20 39 06.59	4.6	
G192.600−00.048	06 12 54.02	17 59 23.32	4.6	
G196.454−01.677	06 14 37.05	13 49 36.16	15.1	
G206.543−16.355	05 41 44.15	−01 54 44.90	12.1	
G209.016−19.398	05 35 13.95	−05 24 09.40	−1.5	
G212.063−00.741	06 47 12.90	00 26 07.00	43.3	
G213.705−12.597	06 07 47.86	−06 22 56.52	10.7	
G232.620+00.995	07 32 09.78	−16 58 12.57	22.7	

Table A.3. 6035 and 6031 MHz OH Zeeman pair candidates identified in the present sample.

Name	LHC V_f (km s^{-1})	LHC S_f (Jy)	RHC V_f (km s^{-1})	RHC S_f (Jy)	V_d (km s^{-1})	B (mG)	Reliability	B_{lit} (mG)
G11.034+00.062	23.93	1.83	23.71	0.92	23.82	−3.9	B	−7.7 [1]; −6.1 [4]
G11.904−00.141	42.76	1.60	42.90	1.00	42.83	+2.5	A	<0.5 [1]; +1.6 [4]
G12.209−00.102	16.96	1.77	17.34	2.00	17.15	+6.8	B	
G12.681−00.182	59.72	1.93	60.39	1.57	60.06	+12.0	B	
G15.035−00.677	21.43	38.29	21.46	29.11	21.45	+0.6	A	<0.5 [1];+1.5 [2];+0.9 [4]
	22.63	19.55	22.63	21.63	22.63	−0.1	A	−0.2 [4]
	23.60	7.53	23.36	3.88	23.48	−4.2	A	−5.4 [4]
	21.53	6.40	21.54	2.85	21.54 [a]	+0.2	A	+0.5 [4]
G25.650+01.049	39.53	2.81	39.25	1.77	39.34	−5.4	A	
G28.201−00.049	94.54	3.05	94.94	3.45	94.74	+7.1	B	+9.0 [2];+6.2 [3];+7.5 [3]
	94.47	0.75	95.02	1.31	94.74 [a]	+7.0	B	
G35.025+00.350	45.27	1.40	45.57	3.23	45.42	+5.4	B	+5.0 [1]
G43.149+00.013	11.15	3.22	10.84	3.03	11.00	−5.5	A	−4.3 [2]
G43.796−00.127	40.18	0.56	40.44	0.59	40.31	+4.6	A	+3.6 [1]
G45.467+00.053	65.03	4.53	64.88	17.02	64.95	−2.8	A	−3.2 [3]
	66.36	12.43	66.29	6.35	66.32	−1.2	A	
	67.71	4.11	68.05	3.31	67.88	+6.0	A	
	65.15	1.76	64.84	1.58	65.00 [a]	−3.9	A	
	66.38	2.26	66.25	0.97	66.31 [a]	−1.6	A	
G48.990−00.299	67.52	1.74	67.64	3.91	67.58	+2.1	A	
G49.490−00.388	52.26	1.72	52.55	1.75	52.40	+5.0	B	+5.0 [2], +3.9 [3]
	54.75	9.05	54.97	10.09	54.86	+3.8	B	
	56.51	3.97	56.77	7.41	56.64	+4.8	A	
	57.65	2.21	57.94	1.99	57.79	+5.3	A	
	62.92	1.55	63.08	2.40	63.00	+2.9	A	
	52.30	4.70	52.67	2.92	52.48 [a]	+4.8	A	
G69.540−00.976	0.02	2.97	−0.55	2.68	−0.27	−10.1	B	−2.7 [3]
	14.52	7.60	14.48	13.41	14.50	−0.9	B	
	14.09	1.77	13.79	2.62	13.94 [a]	−3.8	A	−3.2 [3];−4.2 [3]
G80.861+00.383	−11.02	2.30	−11.18	1.59	−11.10	−2.8	A	−4.3 [3]
	−1.23	1.29	−1.08	2.00	−1.15	+1.6	A	
	−11.02	1.34	−11.25	1.52	−11.13 [a]	−2.9	A	−3.2 [3];−2.7 [3]
G81.871+00.781	7.44	8.63	7.85	13.96	7.65	+7.4	B	+7.8 [3]
	8.67	4.97	9.13	1.47	8.90	+8.3	B	+7.5 [3]
G85.410+00.003	−32.90	0.66	−32.97	1.98	−32.93	−1.2	A	
G98.036+01.446	−62.77	0.58	−62.58	0.58	−62.68	+3.4	B	
	−61.47	1.81	−61.41	1.65	−61.44	+1.1	A	
G108.766−00.986	−44.69	1.05	−45.32	3.89	−45.00	−11.2	B	
	−44.18	1.11	−44.82	1.96	−44.50	−11.4	B	
G111.542+00.777	−59.53	1.37	−59.50	1.11	−59.51	+0.6	B	
G133.947+01.064	−43.33	180.0	−43.00	125.19	−43.17	+5.9	B	
	−43.43	34.57	−42.78	81.54	−43.10 [a]	+8.2	B	
	−42.82	19.97	−42.11	20.25	−42.47 [a]	+9.0	B	

Notes. The peak velocities (V_f) and peak flux densities (S_f) obtained by fitting Gaussian components to the spectra of LHC and RHC features are listed. The demagnetized velocities (V_d), magnetic field strength (B) and estimates of the magnetic field strength from the literature (B_{lit}) are also given. The reliability parameter describes two cases of Zeeman splitting estimation: both polarised spectral features showed single Gaussian components (A) or were blended (B). [a]6031 MHz transition.

References. [1]Caswell & Vaile (1995), [2]Caswell (2003), [3]Baudry et al. (1997), [4]Green et al. (2015).